Microporous and Mesoporous Materials 230 (2016) 1–10

Contents lists available at ScienceDirect

Microporous and Mesoporous Materials

journal homepage: www.elsevier.com/locate/micromeso

Magnetic mesoporous silica for water remediation: Synthesis, characterization and application as adsorbent of molecules and ions of environmental concern

Maximiliano Brigante [a, b, *], Eliana Pecini [a], Marcelo Avena [a, b]

[a] INQUISUR, Departamento de Química, Universidad Nacional del Sur, Av. Alem 1253, 8000 Bahía Blanca, Argentina
[b] Consejo Nacional de Investigaciones Científicas y Técnicas (CONICET), Argentina

ARTICLE INFO

Article history:
Received 9 January 2016
Received in revised form
21 April 2016
Accepted 26 April 2016
Available online 27 April 2016

Keywords:
Magnetic mesoporous silica
Core-shell particles
Solid-water interface
Pollutant adsorption
Electrostatic interactions
Surface complexes

ABSTRACT

Magnetic mesoporous silicas ($NSMSiO_2$) were synthesized by coating nano-sized magnetite (NSM) particles with mesoporous silica shells. The effects of the NSM loading on the morphology, charge development and adsorption properties of the synthesized composites were investigated. Both the shape and the size of aggregates strongly changed as NSM/SiO_2 molar ratio increased, i.e., from plates to spherical-like particles, in agreement with reduction on the silica shell thickness. The shell acted as a protective agent that minimized alteration of the magnetite structure and avoided magnetite dissolution in acidic media. The composites have a significant adsorption capacity towards a humic acid and the cationic dye malachite green, showing that they can adsorb both, anionic and cationic species. HA seems to enter the pores and bind the NSM cores, whereas malachite green binds mainly the silica shell. The effect of Ca^{2+} concentration on the adsorption capacity of the synthesized composite was also evaluated and discussed. The magnetic property of the materials facilitates the recuperation of the adsorbent from aqueous environments.

© 2016 Elsevier Inc. All rights reserved.

1. Introduction

The interactions between environmentally active molecules, such as humic substances, dyes, pesticides, etc. and synthetic adsorbents constitute an area of research of extreme importance in the field of straightforward technological applications as well as in basic science [1]. For example, it is known that the existence of humic acids (HA) in drinking water may lead to color, taste and odor problems, and to biological instability of drinking water in distribution systems. In fact, HA is generally recognized as the major precursor of strongly carcinogenic disinfection by products formed in chlorinated or chloraminated drinking water or water treatment [2]. Another example is the release of dyes and pigments from manufacturing and textile industries. These species are, in general, relatively stable to light, oxidizing agents and heat, and their presence in wastewaters offers considerable resistance to their biodegradation, upsetting aquatic life [3]. Moreover, the dye may enter into the food chain and could possibly cause carcinogenic, mutagenic and teratogenic effects on humans [4].

Because all mentioned species cannot be effectively removed by the conventional treatments used in drinking water supply, it is of great interest to develop effective adsorbents as antidotes or filters for their removal from poisoned circulation systems or contaminated environments. In this respect, mesoporous silica can be a good adsorbent due to its high surface area (>200 $m^2 g^{-1}$), ordered frameworks, narrow pore size distribution (2 − > 10 nm, higher than zeolites), high thermal stability and easy regeneration and reusability [5,6]. Due to these properties, mesoporous silicas are very good base materials for catalysis [7], bioseparation [8], drug delivery [9], medical contrasting [10], food technology [11], biomedicine [12] and separation of environmental pollutants [13]. In fact, it is well documented that the pore morphology of silica and its reactivity towards different molecules strongly depends on the synthesis conditions, e.g., pH, temperature, type and concentration of surfactant used as template, etc. [14].

In order to extend their potential applications, functionalized mesoporous silicas with magnetic iron-based nanoparticles have attracted special attention during the last decade because of their interesting magnetic properties. In addition, it is known that

* Corresponding author. INQUISUR, Departamento de Química, Universidad Nacional del Sur, Av. Alem 1253, 8000 Bahía Blanca, Argentina.
E-mail address: brigante@uns.edu.ar (M. Brigante).

http://dx.doi.org/10.1016/j.micromeso.2016.04.032
1387-1811/© 2016 Elsevier Inc. All rights reserved.

covering the iron core with a silica shell or layer protects it from erosion and oxidation and, thus, increasing its chemical stability [9]. Among all the studied magnetic nanoparticles, nano-sized magnetite (NSM) is one of the most investigated systems due to the broad range of potential applications in various fields, including high-density magnetic recording, ferrofluids, magnetic resonance imaging, and as biomedical materials [15] and adsorbents [16].

As adsorbents, magnetic mesoporous silica composites were used on the remotion of several species, such as DNA, boron, heavy metals, phenols, etc. [8,13,17]. However, the silica shells had to be modified in almost all cases with organic molecules, some of them of a controverted toxicity, in order to increase the adsorption efficiency. In addition, the possible role of the NSM core as adsorbent in the composite has not been yet evaluated.

The aim of this article is to present a study of the synthesis and sorption properties of magnetic mesoporous silicas, prepared by modifying NSM with mesoporous silica. The effects of NSM content of the synthetic composites on the morphology, charge development, sorption of HA and the cationic dye malachite green (MG) are evaluated. Moreover, the adsorption data obtained at a variety of pH, ionic strength and Ca^{2+} concentration are used to gain insights into the mechanisms that govern the adsorption process and into the factors that promote or prevent it. The obtained results will also serve as a basis for further synthesis of new materials for pollution control.

2. Materials and methods

2.1. Chemicals

Cetyltrimethylammonium *p*-toluene sulfonate or tosylate (CTAT, MW = 455.7 $gmol^{-1}$), Pluronic F68 ($PEO_{76}PPO_{29}PEO_{76}$, MW = 8400 $gmol^{-1}$, with PEO and PPO being the poly(oxyethylene) and the poly(oxypropylene) chain units, respectively) and tetraethyl orthosilicate (TEOS, 99%) were purchased from Aldrich. Ferrous chloride tetrahydrate was obtained from Merck. Ferric chloride hexahydrate, hydrochloric acid, nitric acid, sodium hydroxide, calcium chloride and sodium chloride were purchased from Anedra. The HA used for adsorption experiments was extracted from an alfalfa-cultivated soil (INTA Manfredi experimental station, Córdoba, Argentina) and purified according to the procedures recommended by the IHSS. Its elemental composition is C (54.43%), H (4.00%), N (1.62%), and O (39.95%). The ash content of the sample is 1.18% and the total acidity is 9.90 mmol g^{-1} of which 4.71 mmol g^{-1} is ascribed to carboxylic groups and 5.19 mmol g^{-1} to phenolic groups. More information about the general characteristics of this HA sample can be found elsewhere [18]. Malachite green (acetate salt form, MW = 463.5 $gmol^{-1}$) was obtained from Sintorgan. Molecular structures of HA and MG are shown in the Supplementary Material (SM, see SM Fig. S1).

All chemicals were of analytical grade and used as received. Milli-Q water was used for the preparation of solutions.

2.2. Synthesis of materials

2.2.1. Mesoporous silica (SiO_2)

SiO_2 was prepared using a procedure similar to that described in an earlier work [14] with an exception in the method of template removal, i.e., solvent extraction was used here instead of calcination in air furnace as in Ref. [14]. Briefly, 11.6 mL of TEOS were mixed with 2 mL of water and stirred in an autoclave flask for 10 min at 500 rpm. At the same time, 38 mL of Pluronic F68-CTAT mixed solution were prepared with a 1:3 M ratio by adding the desired amount of surfactants to water. This mixed template was stirred in a conical flask at 35 °C to form a transparent solution and then it was left at room temperature. To obtain the mesoporous material, 20 mL of a 1.38 M NaOH solution were added dropwise to the TEOS solution under stirring and 2 min later the surfactant solution was incorporated. The final pH of the mixture was 11.8. The resulting gel, whose composition was 1 TEOS:0.53 NaOH:0.011 CTAT:0.0037 F68, was stirred for 5 min and then left for 48 h in an autoclave at 100 °C. In order to remove the template, the gel was filtered and washed three times with 80 mL of an acidified ethanol solution at 60 °C (400 μL of concentrated HCl solution in 240 mL of a 96% ABV ethanol solution) and then several times with distilled water at room temperature up to neutrality. Finally, the solid was dried at 40 °C overnight.

2.2.2. Nano-sized magnetite (NSM)

NSM was chemically synthesized using a modification of the method described by Illés and Tombácz [19]. Briefly, 100 mL of 0.5 M $FeCl_3$ and 0.275 M $FeCl_2$ solutions were respectively prepared by adding the desired amount of hydrate iron salts to water and bubbled during 30 min with N_2 in order to remove dissolved O_2. Both solutions were mixed and filtered by using 0.2 μm pore-diameter cellulose acetate filters (Osmonic). To obtain the NSM particles, 107 mL of a 2.05 M NaOH solution were added to the iron salts solution in two portions, the first half drop by drop and the second half suddenly under rigorous stirring and N_2 bubbling. The formed black-brown suspension was stirred for a few minutes, and then transferred into 1 L of water. After that, the suspension was washed with water several times to eliminate alkaline impurities from the synthesis and finally acidified with a HCl solution down to pH 3.5 to complete peptization. The stock suspension, whose concentration was determined to be 7.52 g L^{-1}, was stored in the dark at room temperature.

2.2.3. Magnetic mesoporous silica ($NSMSiO_2$)

Three composites with different NSM loading (called $NSMSiO_2$-1, $NSMSiO_2$-2, and $NSMSiO_2$-3) were prepared by adding the desired amount of the dry NSM to the F68/CTAT solution and then sonicating to complete suspension of the material. The resulting suspension was added to the TEOS + NaOH solution, and the system was treated as described for SiO_2. The NSM content of $NSMSiO_2$-1, $NSMSiO_2$-2, and $NSMSiO_2$-3 was 6, 14, and 35%wt., respectively, as measured by UV-VIS spectroscopy using the thiocyanate colorimetric method [20] after extracting the Fe ions from the solid with concentrated HNO_3 [21].

2.3. Characterization of synthesized materials

The synthesized materials were characterized by scanning and transmission electron microscopy (SEM and TEM); XRD; FT-IR spectroscopy; electrophoretic mobility; magnetic measurements; and the N_2-BET method for surface area, pore volume and pore diameter determination. SEM was performed using an EVO 40-XVP microscope. The samples were prepared on graphite stubs and coated with a ca. 300 Å gold layer in a PELCO 91000 sputter coater. TEM was performed using a JEOL 100 CX II transmission electron microscope, operated at 100 kV with magnification up to 450,000 × . Observations were made in a bright field. The powders were placed on 2000 mesh copper supports. XRD patterns were obtained using a Philips PW 1710 diffractometer with CuKα radiation (λ = 1.5406 Å) and graphite monochromator operated at 45 kV, 30 mA and 25 °C; the angle step and counting time were 0.02°(2θ) and 1 s, respectively. FT-IR experiments were recorded in a Nicolet FT-IR Nexus 470 Spectrophotometer. To avoid co-adsorbed water the samples were dried under vacuum until constant weight and then they were diluted with KBr powder before the FT-IR spectra were recorded. The hydrodynamic size and zeta potential of the

materials were measured with a Zetasizer Nano Series instrument (Malvern Instruments Ltd.) at room temperature. Stock suspensions containing 0.1 g L^{-1} of solid in 0 and/or 10^{-2} M NaCl solutions were used for the measurements. The pH of the suspensions was adjusted to the desire value by adding small volumes of HCl or NaOH solutions. The Zeta potential was calculated using the Smoluchowski equation [22]. The magnetic properties of the samples were performed on a LakeShore 7404 vibrating sample magnetometer (VSM) at room temperature under an applied field of 19,000 Oe. The N_2 adsorption isotherms at 77.6 K were measured using the Brunauer–Emmett–Teller (BET) method with a surface area and pore size analyzer (Quantachrome Nova 1200e instrument).

2.4. Adsorption experiments

Adsorption experiments were obtained with a batch equilibration procedure using 15 mL polypropylene centrifuge tubes covered with polypropylene caps immersed in a thermostatic shaker bath. Before starting the experiment, stock HA (1 g L^{-1}) and MG (20 g L^{-1}) solutions were prepared by adding the corresponding solid to water. Its pH was then adjusted to the desired value by adding HCl or KOH solutions. 50 mg of solid were introduced into the tubes and mixed with varying quantities of HA (or MG) and NaCl (used as supporting electrolyte) solutions for 5 h. The range of initial HA and MG concentrations were 0.005–0.1 g L^{-1} and 0.078–7.8 g L^{-1}, respectively, and the final volume was 10 mL. The suspensions were then mixed on a rotator stirrer (FAES, Argentina) for 5 h and the pH was checked and kept constant by adding small volumes (microliters) of concentrated NaOH or HCl solutions. After equilibration, the phases into the tube were separated by centrifugation at 4000 rpm during 10 min and the supernatants were filtered using 0.2 μm pore-diameter cellulose acetate filters prior to quantification. The phase separation was also carried out by using a magnet, mainly with the suspensions where the magnetic adsorbents were present. Adsorbed HA and MG were calculated from the difference between the initial adsorbate concentration and the concentration of the species that remained in the supernatant solution. In most experiments supporting electrolyte was 0.1 M (except when effects of NaCl and/or $CaCl_2$ concentration were investigated) and the working temperature was 25 °C.

Quantification of adsorbates was performed by UV–VIS spectroscopy at 500 nm for HA and at 616 nm for MG using an Agilent 8453 UV–VIS diode array spectrophotometer equipped with a Hellma 1 cm quartz cell. The supernatant of the withdrawn aliquot was placed into the cell and the spectrum was recorded in the 200–900 nm wavelength range. In the case of MG, it is known that the color of the supernatant is stable in the pH range between 3 and 7, but it strongly reduces (up to 70%) at alkaline pH due to structural changes in the dye molecules [23]. Therefore, the supernatant of the withdrawn aliquots at pH 7 and 9.5 were adjusted to pH 4.5 with NaOH or HCl solutions before the absorbance measurement. Calibration curves at the working pH were also constructed with several adsorbate solutions having concentration that ranged between 10 and 200 mg L^{-1} for HA and between 0.13 and 26 mg L^{-1} for MG. Very good linearity was found in all cases ($r^2 > 0.998$).

The adsorption isotherms were fitted using a Langmuir equation, which was commonly used in the adsorption of these molecules on several adsorbent systems [23,24]. The linear form of this equation is displayed as follows:

$$\frac{1}{q_{ads}} = \frac{1}{q_{mon}} + \frac{1}{q_{mon} K_L C_{eq}} \quad (1)$$

where q_{ads} is the adsorbed amount of adsorbate (mg g^{-1}), C_{eq} is the equilibrium concentration of adsorbate in the supernatant (mg L^{-1}), q_{mon} is the maximum amount of molecule adsorbed (mg g^{-1}) corresponding to complete coverage on the surface, and K_L is the Langmuir constant (L mg^{-1}). From the linearized form of Eq. (1), q_{mon}, K_L, and the correlation coefficient, r^2, can be calculated.

The removal efficiency, $R(\%)$, of studied adsorbents was also estimated as follows:

$$R(\%) = \frac{C_{ads}}{C_0} \times 100, \quad (2)$$

where C_{ads} is the adsorbed concentration of the adsorbate at initial concentration C_0.

2.5. Regeneration and reuse of the adsorbent

In order to evaluate both the possibility of regeneration of the adsorbent and its reusability, 10 mL of a 0.04 g L^{-1} HA solution was mixed with 50 mg of mesoporous material. The pH of the solution was previously adjusted to the desired value by adding HCl or KOH solutions. The suspension was then stirred in a 15 mL polypropylene centrifuge tube covered with a polypropylene cap for 5 h. After that, the supernatant was extracted by centrifugation for quantifying the amount of adsorbed HA and the solid was successively washed with a 2.5 × 10^{-3} M NaOH solution with vigorous stirring up to complete desorption of the HA or up to confirm the no appearance of the spectrum by UV-VIS spectroscopy. Higher NaOH concentrations could cause the partial (or complete) dissolution of the amorphous shell [25]. Then, the regenerated adsorbent was thoroughly washed with double-distilled water until a neutral pH was obtained. To be reused in the next cycle of adsorption experiments, the regenerated material was then dried at 60 °C overnight and suspended with the HA solution (0.04 g L^{-1}) at the working pH. The adsorption–desorption cycle was repeated up to three times. Similar experiment was carried out with a 2.34 g L^{-1} MG solution. In this case, the solid was regenerated by sequential washes with a 0.25 M HCl solution and then with double-distilled water up to neutrality. The supporting electrolyte was 0.1 M (NaCl) and the working temperature was 25 °C in all experiments.

3. Results and discussion

3.1. General characteristics of synthesized materials

TEM and SEM micrographs of the synthesized materials are presented in Figs. 1 and 2. According to TEM images, SiO_2 shows a porous structure. It seems to have an arrangement of both ordered and disordered mesopores randomly distributed (Fig. 1a and b). In an earlier paper [6], we reported the synthesis of a well-ordered mesoporous SiO_2, with *p6mm* symmetry (MCM-41), by using the same synthesis technique and chemicals as we employed here, but with calcination for template removal. Since calcination could produce changes in the oxidation state of iron in Fe_3O_4, e.g., transformation to the magnetic maghemite (γ-Fe_2O_3) or to the non-magnetic hematite (α-Fe_2O_3) [8], solvent extraction was used. This process has several advantages in comparison with calcination, for example, it prevents the partial degradation or collapse of the mesoporous structure that can occur in air at relatively high temperatures (>600 °C), it is environmentally friendly (do not produce CO_2 gases and organic amine compounds), and the surfactant can be recycled [26]. One disadvantage of is that it requires several extraction cycles with a high volume of solvent, i.e., if the volume of acidic ethanol is insufficient to remove 100% of the template, a

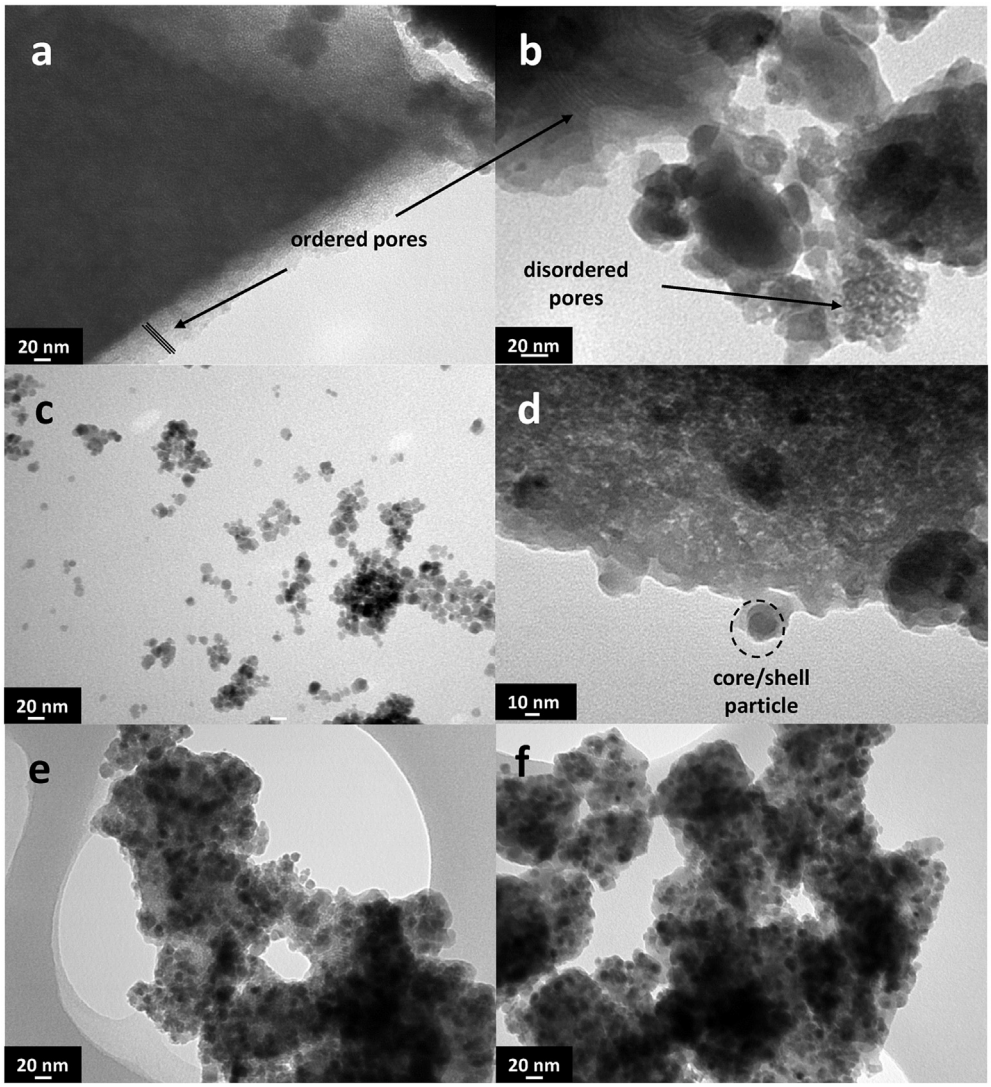

Figure 1. TEM micrographs of the synthesized samples: (a) SiO_2, 450000 × (b) SiO_2, 270,000 × ; (c) NSM, 270000 × ; (d) $NSMSiO_2$-1, 450000 × ; (e) $NSMSiO_2$-2, 270000 × ; and (f) $NSMSiO_2$-3, 270000 × .

significant amount of surfactant will be retained into the pores producing an alteration on the pore structure. This may be the cause of the disordered mesoporous structure found with SiO_2. Fig. 1c shows, on the other hand, that NSM consists of large open aggregates composed of nearly-spherical particles with a narrow size distribution, i.e., the average diameter is around of 12 nm. This is commonly found for this type on nanoparticles [8].

Fig. 1d–f shows pictures of the magnetic mesoporous silicas. Electron dense regions corresponding to NSM particles and less dense regions corresponding to silica are observed, indicating that silica is embedding the magnetic particles forming aggregates of core-shell like particles. Furthermore, NSM appears well disperse and the silica shell preserves the pore structure of bare SiO_2.

According to the SEM images, SiO_2 at low magnification (Fig. 2a) consists of plate-like agglomerates with an average size of around 2.0 μm. At higher magnifications, the material has a sandy granular aspect (Fig. 2b). Similar results were exhibited by $NSMSiO_2$-1 (Fig. 2c). The morphology of the solid changes drastically at higher NSM loadings, i.e., from plate-like to sphere-like agglomerates with a decrease of the agglomerate size (Fig. 2d and e). The average agglomerate size in $NSMSiO_2$-2 and $NSMSiO_2$-3 is around 0.4 and 0.1 μm, respectively. Lim et al. [7] revealed that NSM particles act as seeds by promoting the growth of SiO_2 surrounding the nanoparticles, decreasing consequently the size of the silica domain.

Although not shown here, all composites had a brown color at the naked eye, whose intensity towards dark brown-black increased as NSM content increased.

Fig. 3 shows the XRD patterns of the synthesized samples. NSM shows a typical XRD patterns with reflections at 30.2°, 35.2°, 37.1°, 43.2°, 53.7°, 57.1°, 62.7°, 70.9°, and 74.4° corresponding to the (220), (311), (222), (400), (422), (511), (440), (620), and (533) crystal planes, respectively. The position and relative intensity of all diffraction peaks match well with the standard of the Fe_3O_4 reflections with a cubic inverse spinel structure (JCPDS card 19-0629) [27]. The peak broadening of XRD patterns of Fe_3O_4 indicates the significantly small size of the resulting crystallites. The average crystallite size calculated using Scherrer's equation is 14 nm, close to the value determined by TEM. The broad peak located at 18.4° can be attributed to the formation of amorphous goethite in agreement with the results reported by Iwasaki et al. [28] on the synthesis of NSM by alkaline coprecipitation of Fe(II) and Fe(III) salts at room temperature. This peak camouflages the reflection

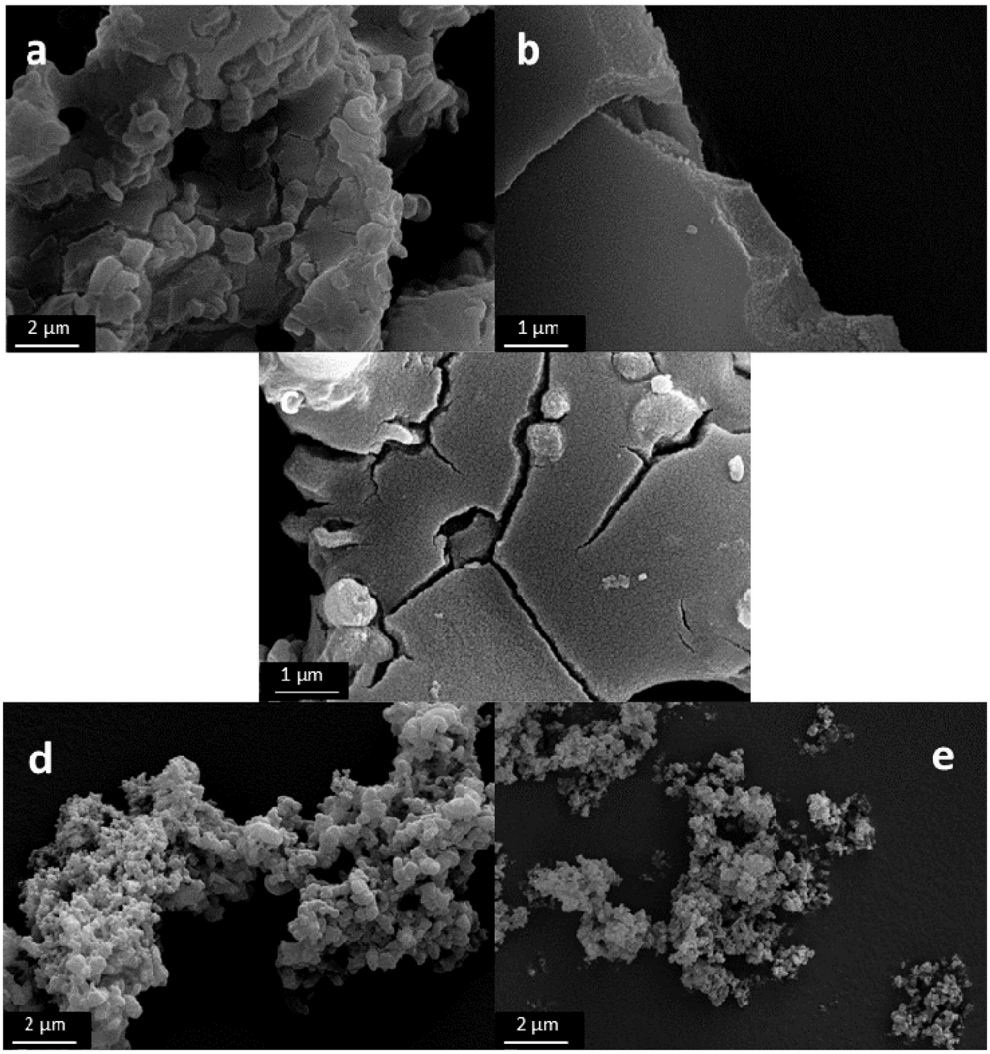

Figure 2. SEM micrographs of the synthesized samples: (a) SiO_2, 20,000 × ; (b) SiO_2, 40,000 × ; (c) $NSMSiO_2$-1, 270000 × ; (d) $NSMSiO_2$-2; and (e) $NSMSiO_2$-3, 270000 × .

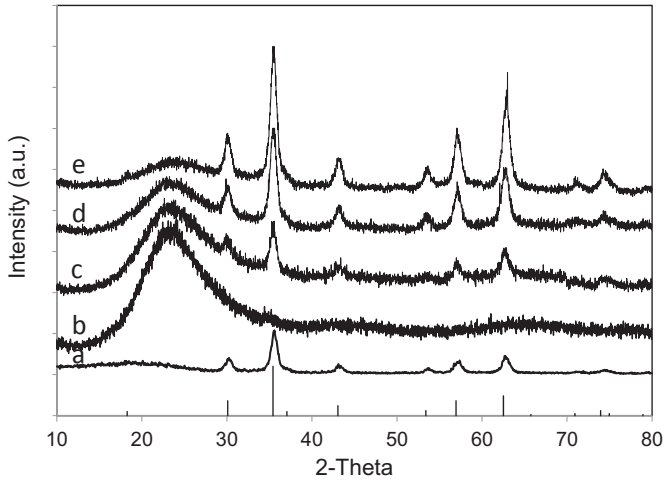

Figure 3. XRD pattern of the synthesized samples at 2-theta range of 10°–80°: (a) NSM, (b) SiO_2, (c) $NSMSiO_2$-1, (d) $NSMSiO_2$-2, and (e) $NSMSiO_2$-3. The lines show the standard position and intensity of the crystalline phase of magnetite (JCPDS 19-0629).

corresponding to the (111) plane of Fe_3O_4. SiO_2 shows a XRD pattern with a broad reflection at $2\theta = 23°$, which is characteristic of amorphous mesoporous silicas [29]. No distinguishable diffraction peaks are detected at lower angles, i.e., it shows a weak and broad peak in the 2°–8° range (data shown in SM Fig. S2) commonly assigned to materials with nonordered mesoporosity or with microporosity [29]. The formation of disordered mesopores was also detected by small angle XRD and reported by Zhang et al. [30] on the synthesis of mesoporous SiO_2 microspheres. Fig. 3 also shows that the intensity of the SiO_2 reflection decreases as NSM/SiO_2 molar ratio increases due to a lower silica content and the composites exhibit the diffraction peaks of the parent NSM, indicating that the magnetite structure is preserved within the silica matrix.

The nitrogen adsorption–desorption isotherms and BJH pore-size distributions of the solids are presented in Fig. 4. The NSM particles show IV-type isotherms according to IUPAC classification and the pore analysis, as shown on the inset of Fig. 4, reveals a broad size distribution attributed to the porosity between particles [31]. The nitrogen sorption isotherms of SiO_2 are typical IV-type isotherms with a sharp increase in volume of adsorbed nitrogen at intermediate P/P_0 which is associated with capillary condensation in mesostructured channels of the solid. Such adsorption

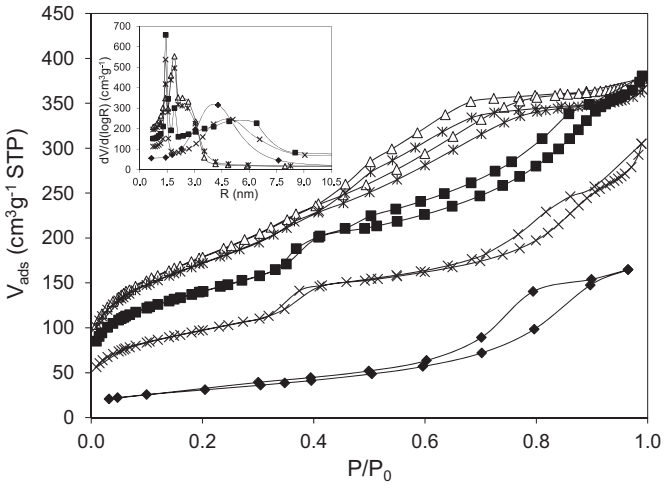

Figure 4. Nitrogen adsorption-desorption isotherms of the synthesized samples: solid diamonds, NSM; open triangles, SiO_2; slashes, $NSMSiO_2$-1; solid squares, $NSMSiO_2$-2; and crosses, $NSMSiO_2$-3. The inset shows the pore size distribution.

behavior is typical of mesoporous materials with narrow pore size distribution [14], although the shoulders in the 1–3 nm pore radius range, as shown in Fig. 4b, may reflect an alteration on the pore structure in agreement with TEM analysis. The hysteresis loop is type H3 which is typical of plate-like particles giving rise to slit-shaped mesopores [32]. Similar results are showed in $NSMSiO_2$-1, revealing that a low NSM content do not alter the mesostructure of SiO_2. On the contrary, each isotherm in $NSMSiO_2$-2 and $NSMSiO_2$-3 has two hysteresis loops in the lower and higher pressure regions, indicating a bimodal pore distribution, one located at 1.4 nm due to mesopores of the SiO_2 network and the other one centered at 5 nm probably due to the presence of pores between the interconnected SiO_2-coated NSM [32,33]. Specific surface area, average pore diameter, and pore volume of the solids are summarized in Table 1. Both the surface area and pore volume of composites strongly decrease as NSM loading increases. These changes are attributed to a lower proportion of SiO_2 in the composite, although the incorporation of Fe_3O_4 nanoparticles into the mesopore structure should not be discarded [33]. On the other hand, the average pore size increases in the order SiO_2 < $NSMSiO_2$-1 < $NSMSiO_2$-2 < $NSMSiO_2$-3 which may be attributed, as mentioned above, to an increased contribution of pores between the interconnected SiO_2-coated NSM. Table 1 also shows the values of hydrodynamic radius of studied samples as measured by dynamic light scattering (DLS). The NSM suspension, prepared in both water and in a 10^{-2} M NaCl solution, consists of particles whose radii is 10–20 times higher than those obtained from TEM and XRD studies. The high value is in agreement to the formation of aggregates in aqueous solution due to a magnetostatic interaction between particles [34]. Moreover, the presence of electrolyte enhances the formation of larger aggregates, mainly if the suspension is near the IEP value of Fe_3O_4 [19]. In the case of SiO_2, the suspension seems to show polydisperse aggregates in 10^{-2} M NaCl, many of which are outside the range measurable by DLS.

Table 1
Nitrogen sorption and DLS results of the synthesized materials.

Sample	A_{BET} (m^2 g^{-1})	D_{aap} (nm)	V_{spat} (cm^3 g^{-1})	D_h (nm)	
				Milli-Q	10^{-2} M NaCl
NSM	108	6.83	0.26	164	427
SiO_2	635	3.65	0.58	396	N/D
$NSMSiO_2$-1	611	3.66	0.56	342	105
$NSMSiO_2$-2	499	4.63	0.53	295	295
$NSMSiO_2$-3	346	5.22	0.45	220	342

Note: A_{BET}: BET surface area; D_{app}: adsorption average pore diameter by BET (8 V/A); V_{spat}: single point adsorption total pore volume of pores; and D_h: hydrodynamic particle diameter by DLS. N/D: not determined.

Fig. 5 shows the FT-IR spectra of synthesized materials. NSM presents a broad band at 3418 cm^{-1} due to the O–H stretching mode and an intense peak at 1630 cm^{-1} due to the O–H bending mode of water molecules. The spectrum clearly depicts the major characteristic absorption bands of Fe_3O_4, at about 581 and 440 cm^{-1} due to Fe–O stretching vibrations in tetrahedral and octahedral positions, respectively. The broadness of the 581 cm^{-1} band is attributed to the formation of nanoparticles [35]. The most important features of the FT-IR spectrum of SiO_2 are: a broad band centered at 3504 cm^{-1} associated to OH stretching of surface hydroxyls bound to silicon; a peak at 1654 cm^{-1} due to the OH bending mode of water molecules; a broad peak located at 1078 cm^{-1} with shoulders at 1195 and 1364 cm^{-1} which are attributed to asymmetric Si–O–Si vibrations; a peak centered at 795 cm^{-1} due to symmetric Si–O–Si vibrations; and peaks at 962 and 465 cm^{-1} assigned to the Si–O–Si bending modes [36]. The apparition of very low intensity peaks (almost negligible) in the 2850–2920 cm^{-1} region, related to aliphatic C–H stretching, could be attributed to a little amount of the organic template that it is not removed during the acid washes of SiO_2 and $NSMSiO_2$ composites. Fig. 5 also shows that the 581 cm^{-1} Fe–O stretching band of Fe_3O_4 is shifted towards lower wavenumbers as NSM/SiO_2 molar ratio decreases, suggesting that NSM particles are in intimate contact with SiO_2 and readily incorporated into the SiO_2 matrix.

The magnetic hysteresis curves of NSM and $NSMSiO_2$ materials are shown in Fig. 6. All samples show a typical superparamagnetic behavior, as evidenced by a negligible value of both the remanence magnetization (<0.1 $emug^{-1}$) and the coercivity field (<0.7 Oe). This observation is expected from the fact that the small size of Fe_3O_4 nanocrystals is used as starting material and there is not particle growth during the synthesis [8], in agreement with TEM images. The magnetic saturation (M_s) of NSM is around of 67 $emug^{-1}$ which is lower than the bulk Fe_3O_4 (ca. 90 $emug^{-1}$) but is comparable with that reported for nano-sized particles [37]. In $NSMSiO_2$ materials the value of M_s strongly decreases as NSM/SiO_2 molar ratio decreases. The gradual loss of magnetization strength can be attributed to the shielding effect of the diamagnetic silica layer [38]. However, it has no significant effect on the magnetic

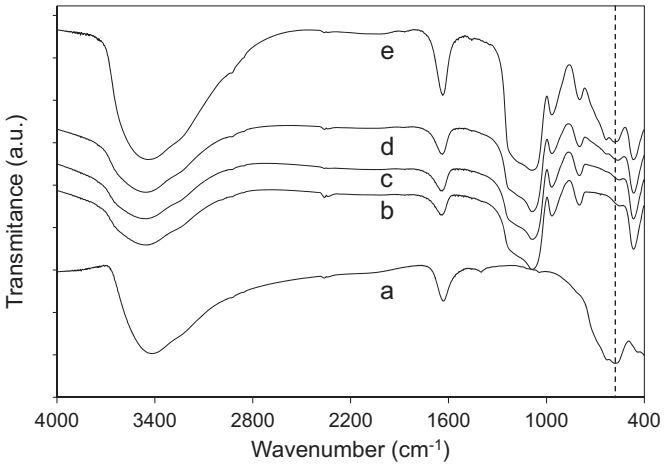

Figure 5. FTIR spectra of the synthesized samples: (a) NSM, (b) SiO_2, (c) $NSMSiO_2$-1, (d) $NSMSiO_2$-2, and (e) $NSMSiO_2$-3. The dotted line is used as a guide.

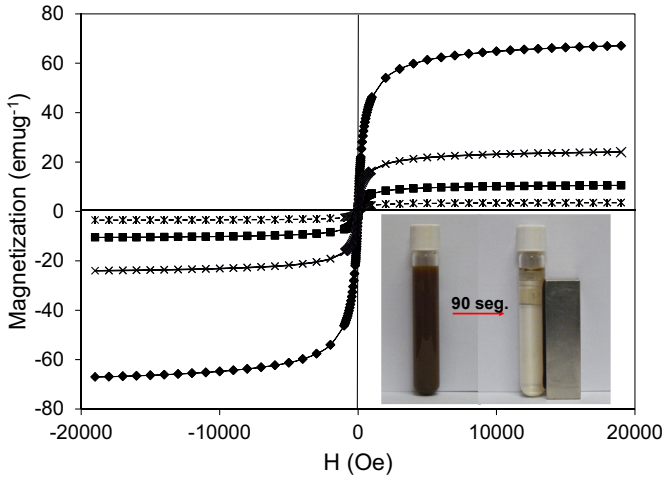

Figure 6. Magnetization curves of synthesized samples: solid diamonds, NSM; slashes, $NSMSiO_2$-1; solid squares, $NSMSiO_2$-2; and crosses, $NSMSiO_2$-3. The inset shows the separation process of $NSMSiO_2$-3 by a magnet.

separability of the material from the bulk solution, as shown in the inset of Fig. 6. In fact, the solid particles were attracted towards the external magnet within a short period (<2 min), demonstrating directly that all composites have magnetic properties. This is important to provide an easy and efficient way of separating the adsorbent from a suspension.

The zeta potential vs. pH data, as shown in Fig. 7, reveals that SiO_2 has an isoelectric point (IEP) of 3.2, which is similar to those obtained for all $NSMSiO_2$ materials. The IEP of bare silica is consistent with those reported in the literature [39]. It is known that the IEP of NSM is between pH 7.5–8.5 [39] in agreement with our results (i.e., IEP = 7.8). Therefore, the fact that all $NSMSiO_2$ composites have the same IEP as SiO_2 indicates that Fe_3O_4 nanoparticles are coated (or encapsulated) by the silica surface and that most of the charging behavior is dominated by silica. To further confirm that NSM particles were indeed coated by silica, the composites were immersed in a 1 M HCl solution. After 3 days immersion, only a negligible amount of iron (as Fe^{3+}) was leached out, indicating that a SiO_2 layer was indeed formed. Similar results were reported by Zhao et al. [13]. The same study was carried out in the bare NSM and it showed the appearance of the typical yellow color of dissolved iron within the first hour of reaction, achieving complete dissolution after 24 h.

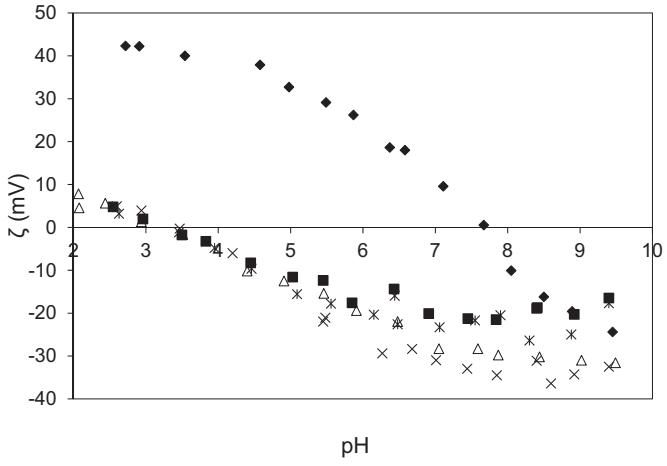

Figure 7. Electrophoretic mobility measurements of synthesized samples as a function of pH: solid diamonds, NSM; open triangles, SiO_2; slashes, $NSMSiO_2$-1; solid squares, $NSMSiO_2$-2; and crosses, $NSMSiO_2$-3.

3.2. Adsorption studies

The removal efficiency of the composites towards HA and MG as a function of the NSM/SiO_2 molar ratio is shown in Fig. 8. The adsorption of HA at pH 4.5 is strongly dependent on the NSM loading, increasing as the NSM/SiO_2 molar ratio increases. Even though the surface area of the composites decreases the adsorption of HA increases. Since it is known that HA molecules (and other organic acids) strongly bind the NSM surface trough the formation of inner sphere complexes between carboxylate groups and ≡Fe–OH surface sites [19,40], the results strongly suggest that some surface of NSM is active and available in the composites for interaction with HA. In fact, the maximum adsorption capacity of $NSMSiO_2$-3, obtained from Eq. (1), is 8.20 mg g^{-1}, almost 5-times higher than that of the bare SiO_2. The increased adsorption by the composite cannot be attributed to the silica shell, which has low affinity for HA molecules, but to the accessibility of humic molecules to the NSM core. Jang, on one side, has reported that the thickness of silica shell is reduced by increasing the NSM/SiO_2 molar ratio [41], which is consistent with TEM images shown in Fig. 1. Suryanarayanan et al. [42] reported, on the other side, that the accessibility of adsorbates to the core is strongly dependent on the porosity of the shell. $NSMSiO_2$-3 has the thinner shell and the largest pores, being thus the composite that better binds HA. The HA increased adsorption at pH 4.5 cannot also be ascribed to changes in surface charge. This is due to that all solids have similar charge development behavior at the studied pH.

Fig. 8 also shows that the all studied materials have high MG adsorption capacity, i.e., the removal efficiency is around 100% in all cases at pH 7. Moreover, the value of q_{mon} in $NSMSiO_2$-3 was calculated to be 542 mg g^{-1}, which is comparable to that obtained by Zheng et al. [43] for the adsorption of MG on granular composite hydrogel, and much higher (up to 10-20 times) than those using natural adsorbents for removal the dye [44]. The adsorption is mainly attributed to electrostatic interactions between the positive-charged functional groups of the dye and the negative-charged silanol groups of the surface of the shell and/or inside the mesopores. Thus, the present results indicate that mesoporous

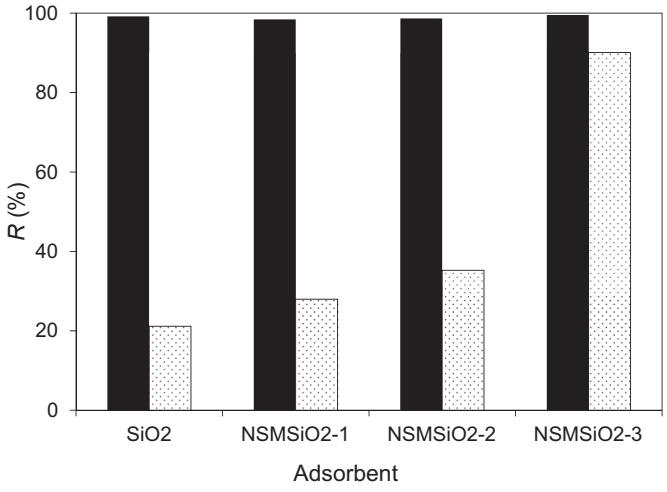

Figure 8. Effect of NSM loading on the removal efficiency of the synthesized solids towards HA at pH 4.5 (dotted bars), and MG at pH 7 (black bars). The initial concentrations of HA and MG are 0.04 and 2.34 g L^{-1}, respectively. NaCl concentration was 0.1 M in all experiments.

SiO_2 can act as a good and potential adsorbent for MG. Although the active solid for MG adsorption is mainly SiO_2, the inclusion of NSM is desirable because it facilitates the recuperation of the adsorbent from aqueous environments (for further regeneration and reuse [33]) by applying a magnetic field.

The direct binding between the adsorbates and the synthesized materials can be interpreted comparing the FT-IR spectra of the solid after adsorption of HA (and MG) and those showed in Fig. 5. The spectra are shown in Fig. 9. The most important features of HA are: a broad band at 3400 cm^{-1} associated to O–H stretching of OH groups, a peak at 2933 cm^{-1} due to aliphatic C–H stretching, a strong peak at 1716 cm^{-1} attributed to C=O stretching of COOH and ketones, a strong peak at 1615 cm^{-1} associated to structural vibrations of aromatic C=C and antisymmetrical stretching of COO^- groups, a medium intensity peak at 1400 cm^{-1} due to symmetrical stretching of COO^- groups and a peak at 1230 cm^{-1} attributed to C–O stretching and OH bending of COOH groups [45]. None of these bands and peaks appear in the FTIR spectra of both SiO_2 after HA adsorption suggesting the low reactivity of SiO_2 shell towards humic substances, which is consistent with the results reported by Zhou et al. [46], and that the adsorption is mainly due to the interaction of HA with the active sites of NSM cores. This is also supported by analyzing the FT-IR spectra of the HA-NSM and HA-$NSMSiO_2$-3 systems shown in Fig. 9a, i.e., the HA peaks located at 1716 and 1400 cm^{-1} shift to lower wavenumbers whereas the band at 1230 cm^{-1} disappears indicating an interaction between the carboxylic (less phenolic) groups of the humic molecules and the ≡Fe–OH surface sites of NSM through to H-bond formations. The peak at 1615 cm^{-1}, related to HA carboxylic groups, seems to be overlapped with the peak of the composite.

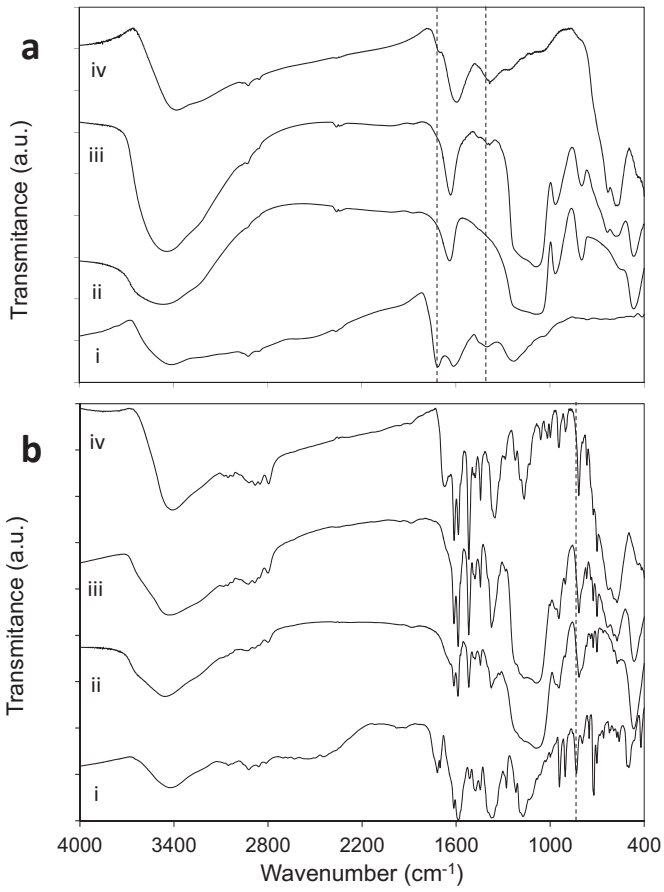

Figure 9. FT-IR spectra of HA (a) and MG (b) before (i) and after adsorption on: SiO_2 (ii), $NSMSiO_2$-3 (iii), and NSM (iv). HA and MG adsorption experiments were carried out at pH 4.5 and pH 7, respectively. NaCl concentration was 0.1 M in all experiments. Dotted lines are used as a guide.

MG has characteristic IR peaks between 1586 and 1615 cm^{-1} due to the C=C stretching of the aromatic ring [47]. It has also peaks in the 670–850 cm^{-1} region related to the C–H bending vibration of benzene, a peak at 1173 cm^{-1} attributed to the C–N stretching vibrations, a peak at 1374 cm^{-1} due to the C–C stretching of the aromatic ring, a peak at 2923 cm^{-1} for C–H stretching of asymmetric CH_3 group, bands located between 2300 and 2700 cm^{-1} corresponding to the symmetric and asymmetric vibration of salt tertiary amine, and two bands between 3200 and 3500 cm^{-1} associated to N–H stretching vibrations of primary amines [47,48]. After adsorption of MG on SiO_2 and $NSMSiO_2$-3, as shown in Fig. 9b, the bands of the dye at 2300–2700 cm^{-1} disappear and the peak at 833 cm^{-1} shifts to lower wavenumbers suggesting a direct binding of the cationic dye to the SiO_2 shell. The binding is mainly due to electrostatic interactions between the cationic MG ($-N^+$) and the deprotonated hydroxyl groups of SiO_2 skeleton ($-Si-O^-$) of the surface and/or inside the mesopores. Similar changes are observed in the MG-NSM system which indicates that the interaction of the dye with the magnetic core should not be discarded [48]. To confirm such hypothesis, other measurements or techniques should be implemented, such as XPS.

The effect of pH, ionic strength and Ca^{2+} concentration on $R(\%)$ of studied adsorbates by $NSMSiO_2$-3 are shown in Fig. 10. The adsorption of HA on the solid strongly decreases as the pH increases (Fig. 10a). It is known that HA molecules in aqueous solution suffer deprotonation of their functional groups by varying the pH, e.g., carboxylic groups deprotonate at pH around 4 or 5 and phenolic groups deprotonate at pH around 9 or 10 [49]. This gives rise to a continuous increase in the negative charge as the pH increases, up to pH above 10 or 11 [49]. In addition, the surface of the composite exhibits negative charges because of deprotonation of surface hydroxyl sites. Therefore, increasing the pH generates, on one side, a decreased number of H-bonds that contribute to hold HA molecules in the solid and, on the other side, an increased electrostatic repulsion between HA and the solid. Both processes contribute to decrease HA adsorption as pH increases. On the contrary, the adsorption of MG on $NSMSiO_2$-3 increases as pH increases. This is due to an increased electrostatic attraction between the positively-charged MG and the increasing negatively-charged $NSMSiO_2$-3. The adsorption experiments performed at pH 9.5 are not reported here due to the partial decomposition and/or degradation of the dye to a less soluble carbinol base via hydroxyl attack [50].

The effect of the ionic strength on $R(\%)$ of studied adsorbates by $NSMSiO_2$-3 is shown in Fig. 10b. The adsorption of HA increases strongly as NaCl concentration increases, and is in line with a decreased electrostatic repulsion between HA and the solid [51]. With respect to MG adsorption, the fact that 100% was adsorbed in all cases indicates that there is a very strong affinity between the adsorbate and the solid, affinity that seems to be not only electrostatic, since changing electrolyte concentration does not modify the high removal.

The effect of the Ca^{2+} concentration on $R(\%)$ of studied adsorbates by $NSMSiO_2$-3 is shown in Fig. 10c. The adsorption of both species is significantly affected by varying the Ca^{2+} concentration from 0 to 10^{-3} M at pH 7. On the one hand, the adsorption of HA strongly increases as Ca^{2+} concentration increases. This increase is mainly attributed to a calcium-bridging mechanism to form ternary HA-Ca^{2+}-SiO_2 complexes being the metal ion an active site for adsorption on SiO_2. Adsorption experiments at Ca^{2+} concentrations higher than 3×10^{-4} M were not carried out due to the surface aggregation and/or precipitation reactions among humic molecules influenced by calcium ions [52]. The formation of calcium bridges

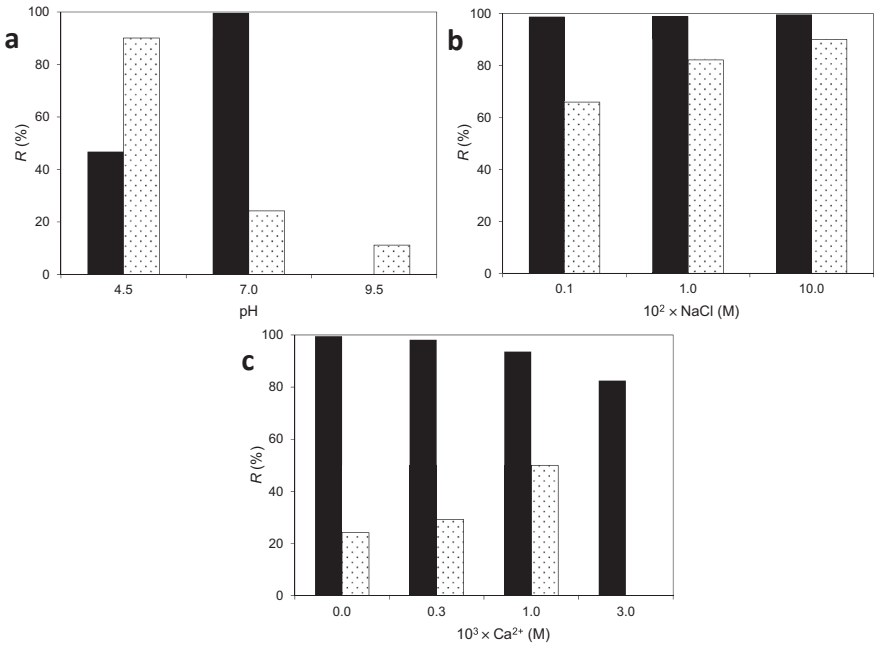

Figure 10. Removal efficiency of $NSMSiO_2$-3 towards HA (dotted bars) and MG (black bars) as a function on: (a) the pH at 0.1 M NaCl; (b) NaCl concentration at pH 4.5 (HA) and pH 7 (MG); and (c) Ca^{2+} concentration at pH 7 and 0.01 M NaCl. The initial concentrations of HA and MG are 0.04 and 2.34 g L^{-1}, respectively.

was also reported on the adsorption of HA on TiO_2, Fe_3O_4 and clay minerals [52–54]. On the other hand, the adsorption of MG strongly decreases as Ca^{2+} concentration increases. The no formation of complexes at pH 7 is indicative of competitive adsorption between MG and the metal ion by the active sites.

3.3. Recycling of the adsorbent

To study the feasibility and practical potential of synthetized $NSMSiO_2$-3 as adsorbent, it was necessary to study the regeneration and reusability of the solid. As a consequence, the removal efficiency in each cycle is shown in SM Fig. S3. On the one hand, the adsorption effectivity towards HA is very good during the studied three cycles, i.e., the effectivity decreases from 90% to 77%. This slightly decrease could be attributed to (a) a little amount of HA that it is still strongly retained by the magnetic core during the alkali washes (pH ~ 11) [54] and decreases the adsorption capacity in the next cycles, and/or (b) changes on the structure of the silica shell due to hydroxyl attack. Both effects cause a decrease of the active sites in the solid. On the other hand, when the material is successively washed with a 0.25 M HCl solution, the MG removal efficiency is excellent after being used four times. Similar results were reported in an earlier paper [6] on the adsorption of the cationic pesticide paraquat on MCM-41. Additionally, Mureseanu et al. [55] reported, by using XRD and FTIR spectroscopy, that the structure of the silica was not altered after three times regeneration by acid treatment.

4. Conclusions

The results shown in this article reveal that the synthesis of magnetic mesoporous silicas produces particles of the type core (NSM) – shell (SiO_2) with significant magnetic and adsorptive properties, suitable for remediation of wastewaters. The solids can adsorb both, the negatively charged HA and the positively charged MG. The adsorption of HA is strongly dependent on the pH, ionic strength and NSM loading. Formation of hydrogen bonds between the functional groups of HA (mainly carboxilic and less phenolic) and the active sites of NSM core are believed to play a key role in the HA adsorption process. To the best of our knowledge, this fact was never demonstrated or discussed in literature. On the other hand, the adsorption of MG is also dependent on the pH, decreasing as the pH decreases. Electrostatic interactions between the cationic dye and the negative-charged silanol groups are relevant, but it seems that other non-electrostatic interactions are also playing an important role. The presence of calcium ions strongly affects the adsorption of HA and MG at neutral pH, i.e., the adsorption of HA increases as Ca^{2+} concentration increases due to the formation of ternary complexes by calcium-bridging whereas the adsorption of MG decreases as Ca^{2+} concentration increases due to the competitive adsorption between the dye and the metal ion by the active sites. Finally, the regenerative study shows that the magnetic adsorbent has good regeneration and reuse after three cycles.

The present results demonstrate that the mesoporous magnetic silica materials can have a great potential application in fast separation and adsorption due to its selectivity, with significant impact on adsorbent-based chemical processes and environmental remediation/cleanup efforts. For example, cationic species (pesticides such as paraquat, dyes like methylene blue, and antibiotics such as tetracyclines) will be mainly adsorbed on the silica shell whereas polar and anionic species (phosphate, arsenate, anionic antibiotics, etc.) will be mainly adsorbed into the magnetic core.

Acknowledgments

This work was financed by SECyT-UNS (PGI UNS 24-Q051), CONICET (PIP 11220110100345) and ANPCYT (PICT 2011-1618). MB and MA are members of CONICET. EP thanks to CONICET for the fellowship granted.

Appendix A. Supplementary data

Supplementary data related to this article can be found at http://dx.doi.org/10.1016/j.micromeso.2016.04.032.

References

[1] A.L.P.F. Caroni, C.R.M. de Lima, M.R. Pereira, J.L.C. Fonseca, Colloids Surf. B 100 (2012) 222–228.
[2] X.R. Zhang, R.A. Minear, Environ. Sci. Technol. 36 (2002) 4033–4038.
[3] P. Janos, H. Buchtova, M. Ryznarova, Water Res. 37 (2003) 4938–4944.
[4] S. Srivastava, R. Sinha, D. Roy, Aquat. Toxicol. 66 (2004) 319–329.
[5] C.T. Kresge, M.E. Leonowicz, W.J. Roth, J.C. Vartuli, J.S. Beck, Nature 359 (1992) 710–712.
[6] M. Brigante, M. Avena, Microporous Mesoporous Mater. 191 (2014) 1–9.
[7] S.H. Lim, E.J. Woo, H. Lee, C.H. Lee, Appl. Catal. B 85 (2008) 71–76.
[8] F. Chen, R. Shi, Y. Xue, L. Chen, Q.H. Wan, J. Magn. Magn. Mater. 322 (2010) 2439–2445.
[9] S. Guo, D. Li, L. Zhang, J. Li, E. Wang, Biomaterials 30 (2009) 1881–1889.
[10] S.H. Wu, Y.S. Lin, Y. Hung, Y.H. Chou, Y.H. Hsu, C. Chang, C.Y. Mou, ChemBioChem 9 (2008) 53–57.
[11] H. Yang, L.W. Ou, A.N. Wimbrow, X.P. Jiang, Y.P. Sun, Int. J. Food Microbiol. 118 (2007) 132–138.
[12] T. Sen, I.J. Bruce, Microporous Mesoporous Mater. 120 (2009) 246–251.
[13] X. Zhao, Y. Shi, T. Wang, Y. Cai, G. Jiang, J. Chromatogr. A 1188 (2008) 140–147.
[14] M. Brigante, P. Schulz, J. Colloid Interface Sci. 369 (2012) 71–81.
[15] A. Lu, E.L. Salabas, F. Schüth, Angew. Chem. Int. Ed. 46 (2007) 1222–1244.
[16] C.H. Weng, Y.T. Lin, C.L. Yeh, Y.C. Sharma, Water Sci. Technol. 62 (2010) 844–851.
[17] M. Santha Moorth, D.-J. Seo, H.-J. Song, S.S. Park, C.-S. Ha, J. Mater. Chem. A 1 (2013) 12485–12496.
[18] N.H. Solá, S.B. Ceppi, R. Sereno, Cienc. Suelo 6 (1988) 108–112 (published in Spanish).
[19] E. Illés, E. Tombácz, J. Colloid Interface Sci. 295 (2006) 115–123.
[20] A.I. Vogel, Textbook of Quantitative Inorganic Analysis, fifth ed., Longmans Scientifical & Technical, London, UK, 1960.
[21] R.M. Twyman, Wet digestion, in: second ed., in: P. Worsfold, A. Townshend, C. Poole (Eds.), Encyclopedia of Analytical Science, vol. 8, Elsevier Science, London, UK, 2005, pp. 146–153.
[22] P. Leroy, C. Tournassat, M. Bizi, J. Colloid Interface Sci. 356 (2011) 442–453.
[23] I.D. Mall, V.C. Srivastava, N.K. Agarwal, I.M. Mishra, Colloids Surf. A 264 (2005) 17–28.
[24] L. Liang, L. Luo, S.Z. Zhang, Colloids Surf. A 384 (2011) 126–130.
[25] Y. Niibori, M. Kunita, O. Tochiyama, T. Chida, J. Nucl. Sci. Technol. 37 (2000) 349–357.
[26] P.T. Tanev, T.J. Pinnavaia, Science 267 (1995) 865–867.
[27] K.C. Souza, G. Salazar-Alvarez, J.D. Aridsson, W.A.A. Macedo, E.M.B. Sousa, Nanotechnology 19 (2008) 185603.
[28] T. Iwasaki, K. Kosaka, N. Mizutani, S. Watano, T. Yanagida, H. Tanaka, T. Kawai, Mater. Lett. 62 (2008) 4155–4157.
[29] T.R. Pauly, T.J. Pinnavaia, Chem. Mater 13 (2001) 987–993.
[30] H. Zhang, J. Wu, L. Zhou, D. Zhang, L. Qi, Langmuir 23 (2007) 1107–1113.
[31] C. Han, D. Zhao, C. Deng, K. Hu, Mater. Lett. 70 (2012) 70–72.
[32] K.M. Ibrahim, H.A. Jbara, J. Hazard. Mater. 163 (2009) 82–86.
[33] M. Xia, C. Chen, M. Long, C. Chen, W. Cai, B. Zhou, Microporous Mesoporous Mater. 145 (2011) 217–223.
[34] J.Y. Park, D. Patel, E.S. Choi, M.J. Baek, Y. Chang, T.J. Kim, G.H. Lee, Colloids Surf. 367 (2010) 41–46.
[35] S. Nasrazadani, A. Raman, Corros. Sci. 34 (1993) 1355–1365.
[36] K. Gude, V.M. Gun'ko, J.P. Blitz, Colloids Surf. A 325 (2008) 17–20.
[37] C. Salazar-Camacho, M. Villalobos, M.L. Rivas-Sánchez, J. Arenas-Alatorre, J. Alcaraz-Cienfuegos, M.E. Gutiérrez-Ruiz, Chem. Geol. 347 (2013) 233–245.
[38] S. Shu, D. Zhang, Z. Chen, Y. Zhang, J. Mater. Chem. 19 (2009) 7710–7715.
[39] M. Kosmulski, J. Colloid Interface Sci. 353 (2011) 1–15.
[40] E. Tombácz, I.Y. Tóth, D. Nesztor, E. Illés, A. Hajdú, M. Szekeres, L. Vékás, Colloids Surf. A 435 (2013) 91–96.
[41] E.S. Jang, J. Korean Chem. Soc. 56 (2012) 478–483.
[42] V. Suryanarayanan, A.S. Nair, R.T. Tom, T. Pradeep, J. Mater. Chem. 14 (2004) 2661–2666.
[43] Y. Zheng, Y. Zhu, A. Wang, Chem. Eng. J. 257 (2014) 66–73.
[44] L. Zhang, H. Zhang, W. Guo, Y. Tian, Appl. Clay Sci. 93–94 (2014) 85–93.
[45] F.J. Stevenson, Humus Chemistry: Genesis, Composition, Reactions, Wiley, New York, 1994.
[46] Y. Zhou, Y. Zhan, P. Li, G. Li, T. Jiang, Powder Technol. 251 (2014) 1–8.
[47] J. Cheria, M. Khaireddine, M. Rouabhia, A. Bakhrouf, Sci. World J. 2012 (2012) 1–9.
[48] A.S. Sartape, A.M. Mandhare, V.V. Jadhav, P.D. Raut, M.A. Anuse, S.S. Kolekar, Arab. J. Chem. (2014) (in press).
[49] C.J. Milne, D.G. Kinniburgh, E. Tipping, Environ. Sci. Technol. 35 (2001) 2049–2059.
[50] Y.C. Lee, J.Y. Kim, H.J. Shin, Sep. Sci. Technol. 48 (2013) 1093–1101.
[51] L. Weng, W.H. Van Riemsdijk, T. Hiemstra, J. Colloid Interface Sci. 314 (2007) 107–118.
[52] N. Kloster, M. Avena, Environ. Chem. 12 (2015) 731–738.
[53] Y. Sun, C. Fan, Prog. Nat. Sci. 11 (2001) 764–765.
[54] J. Fan, F. Liu, Y. Hu, J. Chen, Water Sci. Technol. 72 (2015) 303–310.
[55] M. Mureseanu, A. Reiss, I. Stefanescu, E. David, V. Parvulescu, G. Renard, V. Hulea, Chemosphere 73 (2008) 1499–1504.